Supplementary Materials

Confocal Controlled Raman-LIBS Hybrid Microscope with High Stability and Spatial Resolution

Weiqian Zhao[1], Chunjing He[1], Angze Li[1], Lirong Qiu[1,*] and Ke-mi Xu[1,*]

[1] *MIIT Key Laboratory of Complex-field Intelligent Exploration, School of Optics and Photonics, Beijing Institute of Technology, Beijing 100081, China*.
* Correspondence should be addressed to Lirong Qiu and Ke-mi Xu, qiugrass @126.com; xukemi@bit.edu.cn

This supplementary materials including:

Section I: About the Northwest Africa 13323 Meteorite

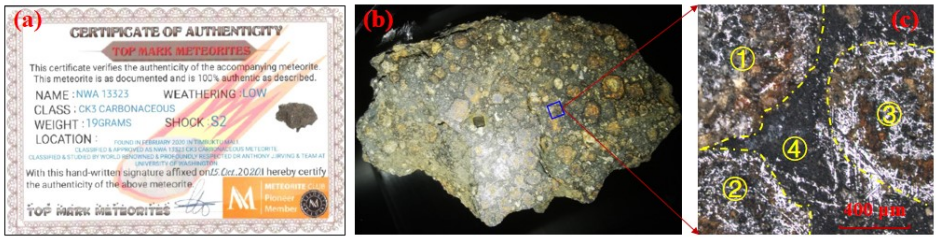

Figure S1. The Northwest Africa 13323 meteorite: (a) certificate confirming authenticity; (b) photograph of cross-section; (c) white-light image of measurement area under a 50× Olympus objective.

Section II: Schematic Diagram of Traditional confocal Hybrid System

Schematic diagram of traditional confocal hybrid system is shown in Figure S2. Compare to confocal controlled Raman-LIBS hybrid system, traditional confocal hybrid system lacks autofocus capability and cannot achieve optimal position excitation. Disadvantage of the system result in low spatial resolution and poor spectral stability, which is extremely important for unknown samples with a complex topography.

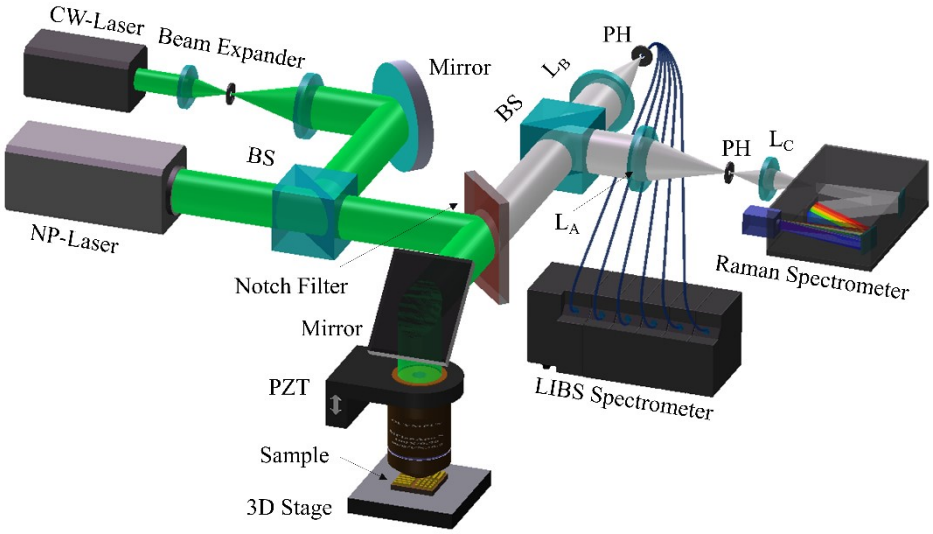

Figure S2. Schematic diagram of traditional confocal hybrid system. NP-Laser, nanosecond pulse Nd:YAG laser; CW-Laser, continuous-wave laser; BS, beam splitter; PZT, piezoelectric ceramic transducer; L_A L_B and L_C, convergent lens; PH, pinhole.

Section III: Spatial Resolution Performance of the System

The spatial resolution of the confocal controlled Raman-LIBS hybrid system includes two indicators: the axial-focusing resolution and the lateral resolution. To prevent the contamination of the objective during acquisition of the LIBS spectrum, an Olympus 50× objective lens (numerical aperture 0.5) was selected to acquire the three-dimensional morphology and spectral information of the meteorite. To further improve the axial-focusing resolution and lateral resolution for morphology imaging, a unilateral-shift-subtracting algorithm [1] has been

introduced into the system.

A silvered mirror was used to characterize the axial-focusing resolution of the system, which is the minimum distance between the two interfaces that the system can distinguish. The objective lens was adjusted to the focus and moved in 15 nm steps in the axial direction, driven by the piezo-actuated objective scanner. The axial-focusing resolutions of the system before and after the introduction of the unilateral translation algorithm are shown in Figure S3(a) and S3(b). Comparing the results, it can be seen that the introduction of the algorithm has been slightly improved the axial-focusing resolution.

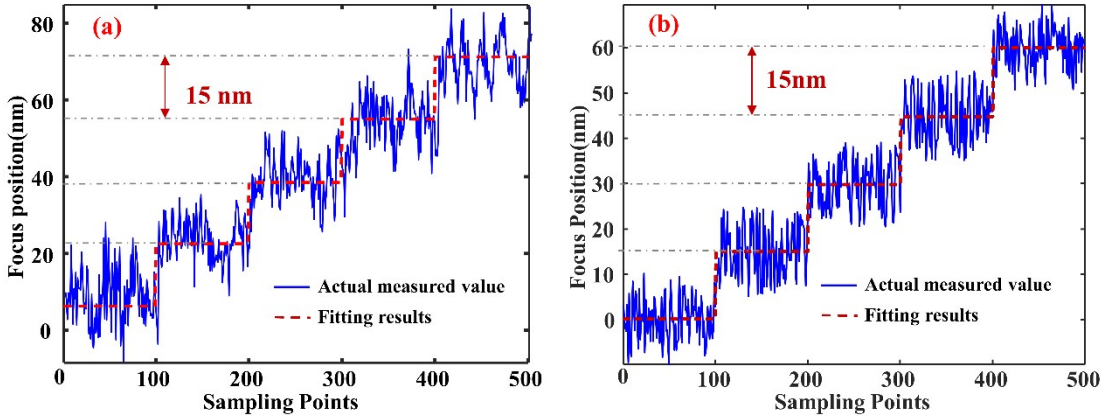

Figure S3. The axial-focusing resolutions of the system (a) before and (b) after the introduction of the unilateral translation algorithm.

In verifying the lateral-resolution performance of the system's morphological imaging, an electron-beam-lithography resolution plate was used as the test sample: the minimum period that could be distinguished was used as the lateral resolution. The lateral resolution of the morphological and component maps of the system are shown in Figure S4. Figures S4(a)-S4(c) show the results by Olympus confocal microscope. Figures S4(d)-S4(f) and S4(g)-S4(i) are the lateral resolution before and after the introduction of the algorithm, respectively. The lateral resolutions of both the morphological and component (Raman shift 520.7 cm^{-1}) maps were 600 nm.

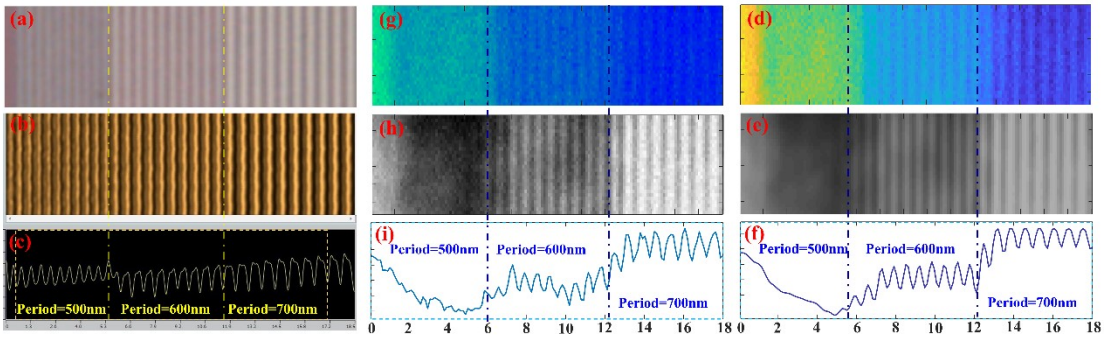

Figure S4. Lateral resolutions of the morphological and component maps: (a) CCD image, (b) laser-intensity image and (c) intensity profile under Olympus confocal microscope; (d) Raman frequency-shift (520.7 cm^{-1}) map, (e) laser-intensity image and (f) intensity profile before the introduction of the algorithm; (g)~(f) the results after the introduction of the

algorithm into the system.

Section IV: Topographic Image Stability Performance of the System

To verify the stability of the confocal controlled system, a standard etched calibration grating was used. The results with a Dimension Icon AFM from Bruker are shown in Figures S5 (a) and S5 (b). The same position of the pattern was measured by the confocal system (Figures S5 (c) and S5 (d)). Comparing the results on the height and period of the pattern, it can be seen that the system can accurately characterize morphology information of the sample.

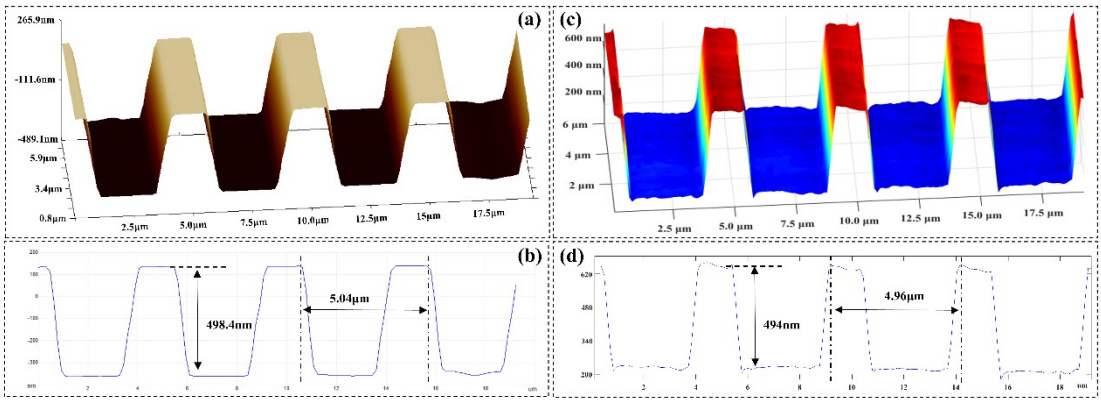

Figure S5. Imaging results of standard etched calibration grating using AFM and confocal controlled systems. (a) height calibration results of AFM; (b) cross-sectional profile of AFM results; (c) 3D profile of the standard grating measured by confocal controlled system; (d) cross-sectional profile of confocal controlled system.

Section V: Assessment of Local Thermodynamic Equilibrium (LTE) and Matrix Effect

According to the McWhirter criterion [2], the necessary condition for LTE is that the ablation transient-plasma electron density $N_e \geq 1.6\times10^{12}(T)^{1/2}(\Delta E)^3$. The electron density can be calculated from the Stark broadening of the atomic emission line by the following formula, with the required parameters extracted from the relevant literature [3]:

$$W_{total} = 2\times W\frac{N_e}{N_e^{ref}} \quad \text{(S1)}$$

Where N_e is the electron density; Nref e is the reference electron density, 10^{16} cm^{-3}; W is half of the full width at half maximum of the electron collision peak (0.54 for the 288.14 nm peak of Si I); W_{total} is the spectral line broadening caused by the Stark effect.

For the calculation of the electron density, the Stark broadenings were extracted using Voigt-profile fitting functions containing Gaussian broadening contributions from the spectrometer resolution [4]. According to the above protocol, the calculated electron densities of the laser-ablation transient plasma were within the range $1.0\times10^{16}\sim1.5\times10^{16}$ cm^{-3}. Such a N_e fulfills the critical electron densities condition estimated by the McWhirter's criterion, which is necessary to ensure the

LTE.

Prior to elemental mapping, the matrix effect must be assessed by measuring the electron densities and temperatures of the plasmas. Boltzmann plots were therefore drawn to extract the excitation temperatures of the sample points [5]. Atomic Fe lines used for the calculation of the excitation temperature are shown in Table S1.

Table S1. Parameters used for plasma temperature calculation.

Ion	λ (nm)	g_kA_{ki} (s^{-1})	E_i (cm^{-1})	E_k (cm^{-1})	Lower Level	Upper Level
Fe I	293.789	1.26E+08	0.0000	4.2204	$3d^64s^2$	$3d^7(^4F)4p$
Fe I	302.248	9.70E+07	0.0873	4.1909	$3d^64s^2$	$3d^6(^5D)4s4p(^3P)$
Fe I	344.179	1.20E+08	0.0000	3.6025	$3d^64s^2$	$3d^6(^5D)4s4p(^3P)$
Fe I	357.005	3.86E+08	0.9582	4.4346	$3d^7(^4F)4s$	$3d^7(^4F)4p$
Fe I	361.851	5.05E+08	0.9901	4.4153	$3d^7(^4F)4s$	$3d^7(^4F)4p$

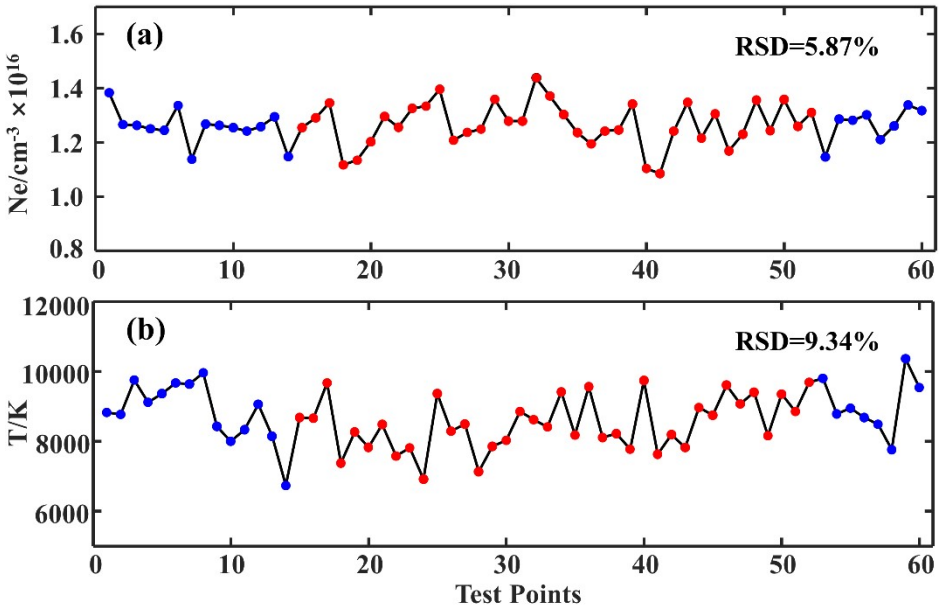

Figure S6. Distribution of (a) electron density N_e and (b) excitation temperature T(K) in the linear profile of the Northwest Africa 13323 meteorite. Red: spherulites data; Blue: carbon material data.

The results shown in Figure S6 illustrate random dispersions of the electron densities and the temperatures along the linear profile of Northwest Africa 13323, suggesting no correlation exists between these observables and the meteorite materials. Then, relative standard deviation (RSD) is used to characterize fluctuations in electron density and excitation temperature. The measured electron density and the excitation temperature show fluctuations of 5.81% and 9.34% respectively. Such relative standard deviation (RSD) values indicate that the meteorite was in a LTE state with negligible matrix effects.

Section VI: Typical LIBS spectral lines for the meteorite

Table S2. Typical LIBS spectral lines for the meteorite.

Number	Ion	λ (nm)	Number	Ion	λ (nm)
1	Mg I	285.17	15	Mg I	383.224
2	Si I	288.14	16	Mg I	383.853
3	Fe I	293.69	17	Ca II	393.363
4	Fe I	298.671	18	Al I	394.397
5	Fe I	302.16	19	Al I	396.184
6	Al I	308.374	20	Ca II	396.870
7	Al I	309.505	21	Fe I	404.576
8	Ca II	316.105	22	Fe I	406.336
9	Ca II	318.185	23	Fe I	407.214
10	Fe I	344.179	24	Ca I	422.687
11	Fe I	357.005	25	Ca I	430.799
12	Fe I	358.084	26	Fe I	438.350
13	Fe I	361.851	27	Fe I	440.461
14	Fe I	371.486	28	Ca I	445.484

Section VII: Original Complex Raman Spectrum of the Northwest Africa 13323 Meteorite

The size of the meteorite measurement area is 1280 μm × 1280 μm, and the sample-point distance is 10 μm, so the number of sample points is 128 × 128. The original complex Raman spectrum of the meteorite totals 16384, so it is difficult and confusing to draw all complex spectra of meteorites. To make the graph more concise, we randomly select 300 spectra to represent the original complex Raman spectrum of the meteorite. The original complex Raman spectrum are shown in Figure S7.

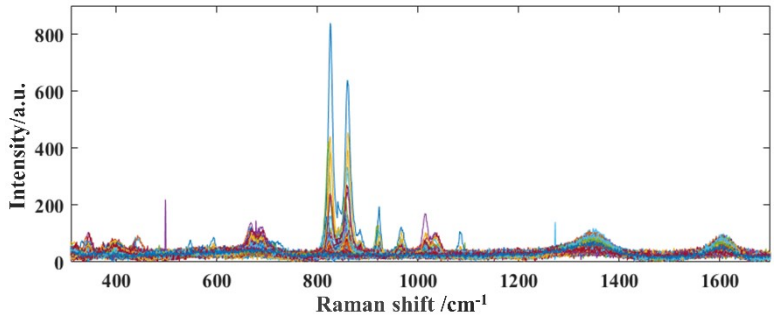

Figure S7. The original complex Raman spectrum of the meteorite.

Section VIII: Spectral-mapping Reconstruction Performance of Confocal Controlled System and Traditional Confocal System

To characteristic spectral-mapping reconstruction performance of confocal controlled system and traditional confocal system, another area of the NWA13323 carbonaceous chondrite was used for experiments. A CCD image (under the 10× Olympus objective) of the meteorite with a size of 1280 μm × 1280 μm is shown

in Figure S8(a). From the CCD image: the main area of the meteorite is a spherulites surrounded by carbonaceous material. 3D profile of the meteorite measured by confocal controlled system is shown in Figure S8(b), from which it can be seen that the maximum undulating height difference is about 50 μm. Typical Raman spectral are shown in Figure S8(c). These peaks can be assigned to the characteristic Raman transitions of carbon (D-band at 1345.6 cm^{-1} and G-band at 1602 cm^{-1}), pyroxene (399, 655.8, and 1017.6 cm^{-1}) and olivine (826.1 and 885.3 cm^{-1}).

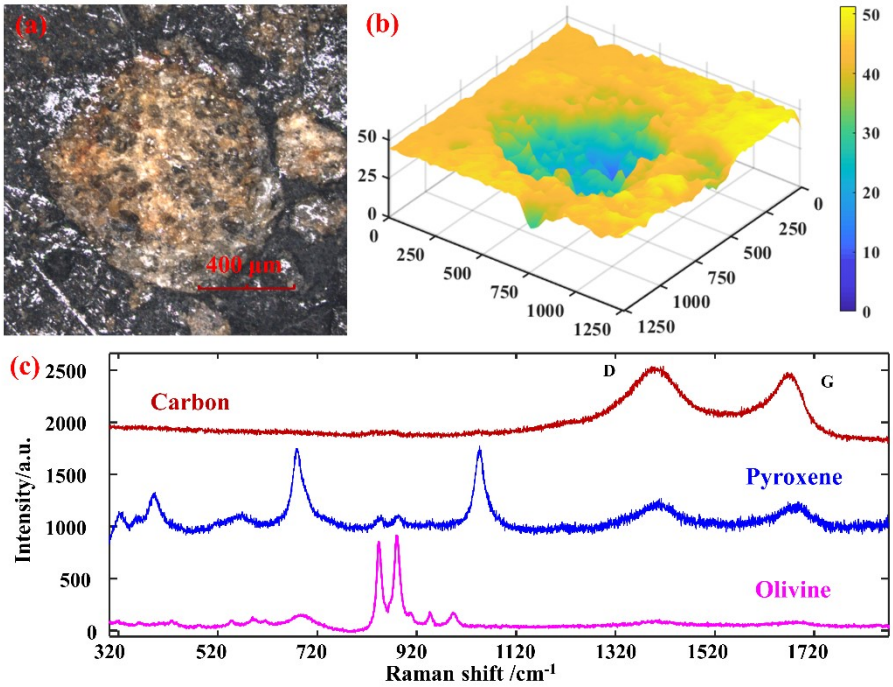

Figure S8. (a) CCD image (size: 1280 μm × 1280 μm) of the meteorite under the 10× Olympus objective. (b) 3D profile of the meteorite measured by confocal controlled system. (c) Typical Raman spectral of the meteorite NWA13323.

Figures S9(a), S9(c) and S9(e) show the distributions of pyroxene, olivine, and carbon under confocal controlled system. Figures S9(b), S9(d) and S9(f) show the distributions under traditional confocal system. The results show that traditional confocal system has deviations in spectral signals due to defocusing acquisition. The confocal controlled system provides high-precision autofocus and spectral information, which is essential for complex morphology samples.

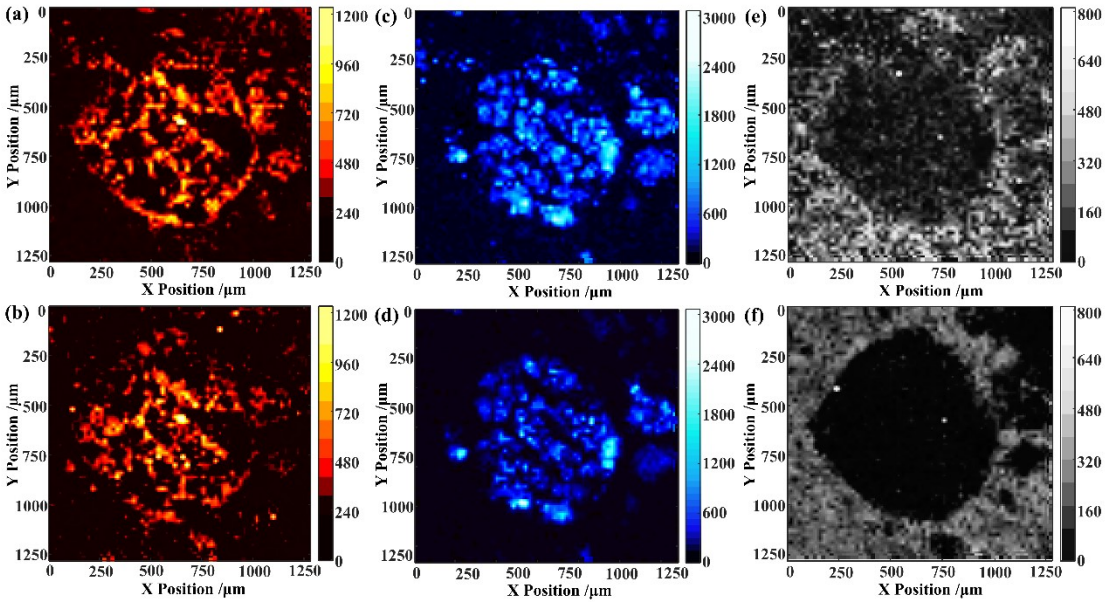

Figure S9. Distributions of pyroxene ((a) and (b)), olivine ((c) and (d)), and carbon ((e) and (f)) measured by confocal controlled system and traditional confocal system.

Section X: Peak-metamorphic-temperature of the Meteorite under the Confocal Controlled System and Traditional Confocal System

Based on the Raman spectra measured by confocal controlled system and traditional confocal system in Section V, we intercept the 1200-1800 cm^{-1} range for analysis. The width of the D band obtained from the fits was used to calculate T_{EFF}.

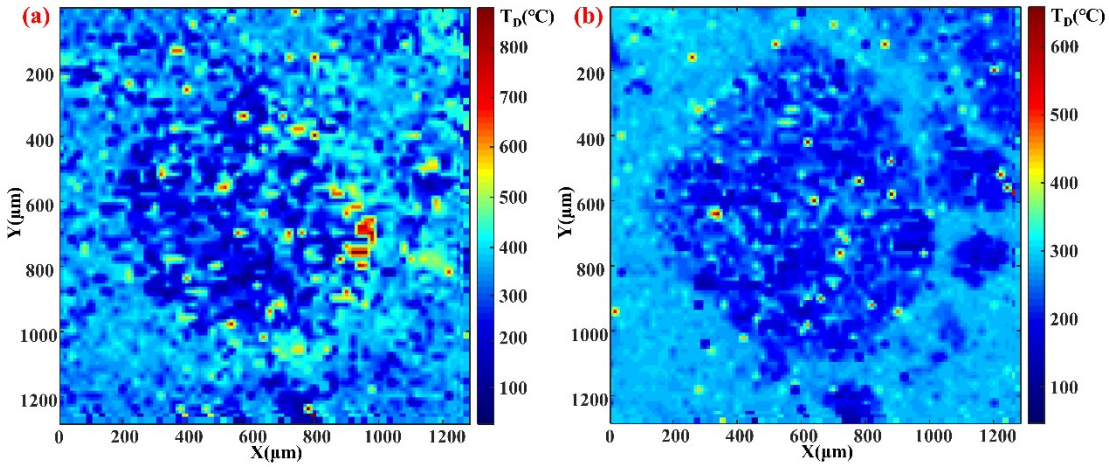

Figure S10. Peak-metamorphic-temperature of the meteorite under (a) confocal controlled system and (b) traditional confocal system.

Peak-metamorphic-temperature of the meteorite under the confocal controlled system and traditional confocal system are shown in Figures S10(a) and S10(b), respectively. Compared with traditional confocal system, confocal controlled system can obtain more detailed about peak-metamorphic-temperature. Traditional confocal system collects spectral at non-focus positions, resulting in inaccurate judgment of the temperature. Therefore, confocal controlled system

can improve the accuracy of spectral, thereby improving the accuracy of meteorite thermal metamorphism analysis.

References

[1] Sun, Y. B.; Zhao, W, Q.; Wang, Y.; Li, R. Unilateral-shift-subtracting confocal microscopy with nanoscale axial focusing precision. *Appl. Optics*. **2018**, 57(30), 8876-8886.

[2] Cristoforetti, G.; De Giacomo, A.; Dell'Aglio, M.; Legnaioli, S.; Tognoni, E.; Palleschi, V.; Omenetto, N. Local thermodynamic equilibrium in laser-induced breakdown spectroscopy: beyond the McWhirter criterion. *Spectrochim. Acta. B*. **2010**, 65(1), 86-95.

[3] Aguilera, J. A.; Aragón, C. Characterization of laser-induced plasmas by emission spectroscopy with curve-of-growth measurements. Part I: Temporal evolution of plasma parameters and self-absorption. *Spectrochim. Acta. B*. **2008**, 63(7), 784-792.

[4] Djenize, S.; Sreckovic, A.; Jelisavcic, M.; Bukvic, S. Experimental Stark widths and shifts of triply ionized sulfur spectral lines. *Astron. Astrophys*. **2002**, 389(1), 1086-1089.

[5] Mohamed, W. T. Y. Study of the matrix effect on the plasma characterization of six elements in aluminum alloys using LIBS with a portable echelle spectrometer. *Prog. Phys*. **2007**, 2(2), 46-52.